Nuclear Lattice Effective Field Theory: Status A.D. 2022

U.-G. Meißner

published in

NIC Symposium 2022
M. Müller, Ch. Peter, A. Trautmann (Editors)

Forschungszentrum Jülich GmbH,
John von Neumann Institute for Computing (NIC),
Schriften des Forschungszentrums Jülich, NIC Series, Vol. 51,
ISBN 978-3-95806-646-5, pp. 97.
http://hdl.handle.net/2128/31840

Nuclear Lattice Effective Field Theory: Status A.D. 2022

Ulf-G. Meißner[1,2,3]

[1] Helmholtz-Institut für Strahlen- und Kernphysik and Bethe Center for Theoretical Physics, Universität Bonn, 53115 Bonn, Germany
E-mail: meissner@hiskp.uni-bonn.de

[2] Institute for Advanced Simulation (IAS-4) and Institut für Kernphysik (IKP-3), Forschungszentrum Jülich, 52425 Jülich, Germany

[3] Tbilisi State University, 0186 Tbilisi, Georgia

I discuss recent developments in nuclear lattice effective field theory, which is a premier tool in the theory of nuclear structure and reactions. I discuss a number of exciting results on topics such as nuclear thermodynamics, perturbative nuclear structure calculations beyond first order perturbation theory and a three-dimensional tomography of the carbon nucleus. I also discuss alpha-alpha scattering in the multiverse and give an outlook on upcoming results at N3LO precision.

1 Introduction

Understanding the formation of strongly interacting systems such as atomic nuclei from first principles calculations is still one of the biggest challenges within contemporary theoretical physics. While the theory of the strong interactions, Quantum Chromodynamics (QCD), is well tested in many processes, the matter that leads to life in our Universe is based on nuclei, which are self-bound systems of nucleons (protons and neutrons). As the nucleons themselves consist of quarks and gluons, and hence are not fundamental degrees of freedom, the forces between nucleons are not completely given in terms of two-body interactions, but include three-body and higher order interaction terms. Much progress in the understanding of the structure and dynamics of nuclei has been made in the context of Nuclear Lattice Effective Field Theory (NLEFT)[1], which combines the so successful low-energy chiral effective field theory of QCD with stochastic methods (Monte Carlo simulations). While direct calculations of nuclei based on quarks and gluons in the framework of lattice QCD are essentially impossible due to the severe sign problem, formulating the nuclear forces in terms of protons, neutrons and pions is not only more appropriate, but also comes with the added value of the approximate Wigner SU(4) (spin-isospin) symmetry of the underlying nuclear interactions. This symmetry in fact suppresses the sign oscillations strongly, and in the limit of an exact Wigner SU(4) symmetry, spin-isospin saturated nuclei like e.g. ^{4}He are free of any sign oscillation. In NLEFT simulations, Euclidean space-time is discretised on a torus of volume $L^3 \times L_t$, where L is the side length of the spatial dimension, and L_t denotes the extent of the Euclidean time dimension. The lattice spacing in the spatial (temporal) dimensions is a (a_t). The maximal momentum on the lattice is $p_{\rm max} \equiv \pi/a$, which serves as the UV regulator of the theory. Nucleons are point-like particles on the lattice sites, and the interactions between nucleons (pion exchanges and contact terms) are treated as insertions on the nucleon world lines via auxiliary-field representations. Properties of multi-nucleon systems are computed by means of the projection Monte

Carlo (MC) method. Each nucleon is treated as a single particle propagating in a fluctuating background of pion and auxiliary fields. Both local and non-local smearings are applied to the nucleon creation and annihilation operators. Euclidean time projection is started from some initial state Ψ_A for Z protons and N neutrons (with $A = Z + N$). Then, a Wigner SU(4) symmetric Hamiltonian is used as a computationally inexpensive filter for the first few Euclidean time steps. This suppresses sign oscillations dramatically. Finally, the full LO chiral EFT Hamiltonian is applied and one calculates the ground state energy and other properties from the correlation function $Z(t) \equiv \langle \Psi_A | \exp(-tH) | \Psi_A \rangle = \mathrm{Tr}\{M^{L_t}\}$, in the limit of large Euclidean projection time t, with M the normal-ordered transfer-matrix operator and L_t the number of Euclidean time steps. Higher-order contributions are computed as perturbative corrections to the LO amplitude. The properties of excited states are obtained from a multi-channel projection MC method. Further, lattice improvement and smearing is applied to the momentum-dependent operators and operators are included, that allow to remove the artifacts from the breaking of rotational symmetry on the lattice. A much more detailed description is given in the recent monograph[1].

2 Nuclear Thermodynamics

The equation of state of strongly interacting matter is one of the central topics in contemporary nuclear physics, as it plays an important role in the early universe and the generation of gravitational waves in neutron star mergers. There are also important connections between the nuclear equation of state and heavy-ion collisions. It is well established that highly-excited nuclear states can be treated statistically as part of an equilibrium thermal distribution. The large density of states at high energies allows a treatment in terms of thermodynamical concepts, such as temperature, entropy, and free energy. Within NLEFT a new paradigm for calculating *ab initio* nuclear thermodynamics for lattice simulations was developed in Ref. 2. This is based on a new and efficient method, called the pinhole trace algorithm (PTA), for computing nuclear observables at nonzero temperature using a canonical ensemble with fixed numbers of protons and neutrons. For a canonical ensemble with fixed nucleon number A, volume $V = L^3$ and temperature T, the expectation value of any observable $\mathcal{O}$ is given by

$$\langle \mathcal{O} \rangle_\beta = \frac{Z_\mathcal{O}(\beta)}{Z(\beta)} = \frac{\mathrm{Tr}_A(e^{-\beta H}\mathcal{O})}{\mathrm{Tr}_A(e^{-\beta H})}, \tag{1}$$

with $Z(\beta)$ the partition function, $\beta = T^{-1}$ the inverse temperature, H the Hamiltonian, and Tr_A is the trace over the A-body Hilbert space. Throughout, canonical units with $\hbar = c = k_B = 1$ are utilised. The PTA can be used to efficiently compute $Z(\beta)$ and $Z_\mathcal{O}(\beta)$ on the lattice. The PTA is an extension of the pinhole algorithm introduced in Ref. 3 to sample the spatial positions and spin/isospin indices of the nucleons. The new feature is that a quantum mechanical trace over all possible states is performed in addition. The partition function $Z(\beta)$ can be written explicitly in the single particle basis as

$$Z(\beta) = \sum_{c_1,\cdots,c_A} \langle c_1, \cdots, c_A | \exp(-\beta H) | c_1, \cdots, c_A \rangle, \tag{2}$$

where the basis states are Slater determinants composed of point particles, $c_i = (\boldsymbol{n}_i, \sigma_i, \tau_i)$ which combine the lattice vector of the i-th particle, its spin σ_i i and isospin τ_i. The neutron

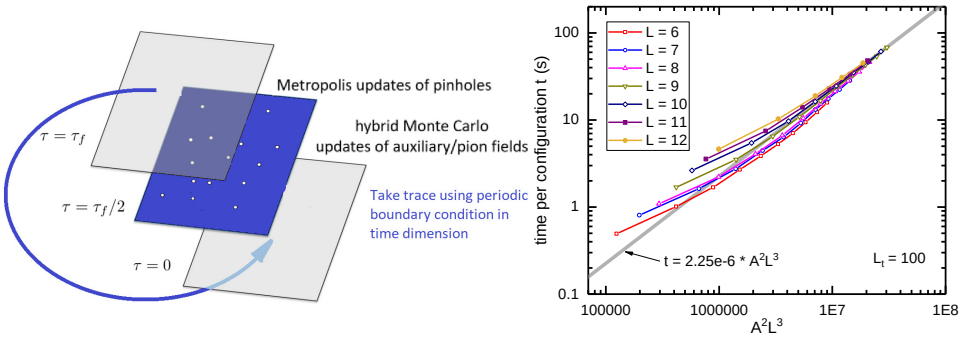

Figure 1. Left panel: The pinhole trace algorithm (PTA). At mid-times $t = L_t a_t/2$, a sheet with pinholes of spin-isospin indices $(i_n j_n)$ is inserted and the periodic boundary conditions impose the temperature $\beta = 1/T$. Right panel: Scaling of the PTA with nucleon number A and volume $V = L^3$.

number N and proton number Z are separately conserved, and the sum in Eq. 2 is limited to the subspace with the specified values for N and Z. By decomposing the interactions in H using auxiliary fields, one obtains the path-integral expression for Eq. 2

$$Z(\beta) = \sum_{c_1,\cdots,c_A} \int \mathcal{D}s_1 \cdots \mathcal{D}s_{L_t} \langle c_1, \cdots, c_A | \, M(s_{L_t}) \cdots M(s_1) | c_1, \cdots, c_A \rangle, \quad (3)$$

with the $M(s_{n_t})$ the normal-ordered transfer matrix for time step n_t, and s_{n_t} is a shorthand notation for all auxiliary fields at that time step. In the PTA one evaluates Eq. 3 using Monte Carlo methods, see the left panel of Fig. 1 for a graphical illustration and more details are given in Ref. 2. The arguably biggest advantage of the PTA is its time scaling $\sim A^2 V L_t$, see the right panel of Fig. 1. This is very different to commonly used algorithms based on the grand-canonical ensemble, like the well-known BSS method first described in Ref. 4. The BBS algorithm scales as $AV^2 L_t$, so the cost savings of the PTA is a factor of V/A. Thus, the speedup associated with the PTA can be as large as one thousand, depending on the lattice spacing and particle density. Another important technical aspect related to the calculation of thermodynamic quantities is the use of twisted boundary conditions (TBCs). The finite volume together with the chosen boundary condition will induce fictitious shell effects. The origin of the finite volume shell effects is the constraint imposed by the boundary conditions on the particle momenta. One way to overcome this is to use TBCs[5]. Here, extra phases are attached to the wave function when a particle cross the boundaries. Averaging over all possible twist angles provides an efficient way of approaching the infinite volume limit[6–9,2]. In Ref. 2 simulations to investigate the nuclear liquid-vapour phase transition were performed on $L^3 = 4^3, 5^3, 6^3$ cubic lattices with up to 144 nucleons and a spatial lattice spacing $a = 1.32$ fm, such that the corresponding momentum cutoff is $\Lambda = \pi/a \approx 471$ MeV. The temporal lattice spacing is taken to be $a_t = 1/2000$ MeV^{-1}. The temperatures considered spanned the range from 10-20 MeV and the densities varied from $n = 0.008$ fm^{-3} to $n = 0.20$ fm^{-3}. Remember that nuclear matter density is $n_0 = 0.16$ fm^{-3}. These settings allow one to explore the whole region relevant to the nuclear matter liquid-vapour phase transition. Throughout, symmetric nuclear matter with $N = Z$ and without the Coulomb interaction was considered. In Fig. 2 the calculated chemical potential and pressure isotherms are

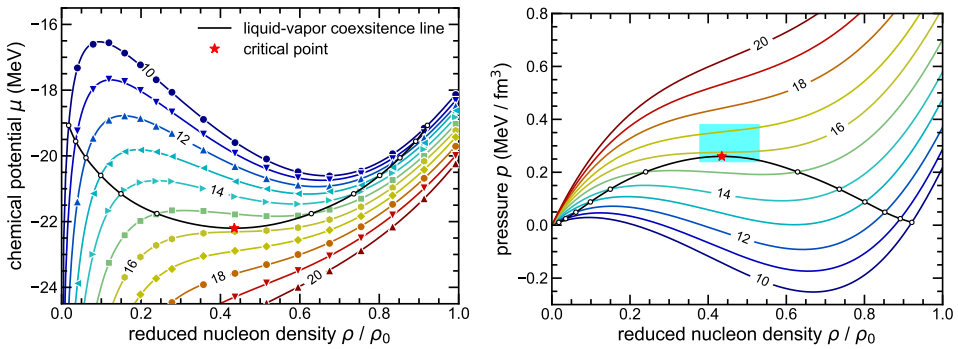

Figure 2. Left panel: The μ-ρ isotherms of symmetric nuclear matter in a volume $L^3 = 6^3$. The numbers on the lines are temperatures in MeV. The black line denotes the liquid-vapour coexistence line derived from Maxwell construction, and the red star marks the calculated critical point. Right panel: The p-ρ isotherms of symmetric nuclear matter for $L^3 = 6^3$. The black line denotes the liquid-vapour coexistence line, and the red star marks the calculated critical point. The cyan rectangle marks the empirical critical point extracted from heavy-ion collisions[10].

shown. Each point represents a separate simulation. All the MC errors for μ are smaller than 0.02 MeV and not shown explicitly. The critical point is then deduced from solving the equations $d\mu/d\rho = d^2\mu/d\rho^2 = 0$. The uncertainties in the critical values are estimated by propagating the simulation and interpolation errors. The critical temperature, density, and chemical potential are, in order: $T_c = 15.80(3)$ MeV, $\rho_c = 0.089(1)$ fm^{-3}, and $\mu_c = -22.20(1)$ MeV. The liquid-vapour coexistence line is determined through the Maxwell construction of each isotherm and depicted as a solid black line in Fig. 2. All the other bulk thermodynamic quantities can be reliably extracted based on the calculated high-precision energies and chemical potentials. In the right panel of Fig. 2 the deduced pressure-density isotherms are shown as well as the corresponding liquid-vapour coexistence line and the critical point. The calculated critical pressure is P_c =0.260(3) MeV/fm^3. For comparison, the critical point extracted by analysing the cluster distributions in heavy-ion collisions, $T_c = 17.9(4)$ MeV, $\rho_c = 0.06(1)$ fm^{-3} and $P_c = 0.31(7)$ MeV/fm^3 is also shown[10]. Note that these calculations employ a leading-order chiral interaction which slightly overestimates the nuclear matter saturation density ρ_0, which leads to a systematic error of about 10%. Thus, the quality of both ρ_0 and ρ_c calculations can be improved by including higher-order corrections. Note that the calculated isotherms follow exactly the pattern expected for a liquid-vapour phase transition in a finite system. Above T_c the system is in a supercritical state, while below T_c the pure liquid and vapour phases exist in the high- and low-density regime, respectively. For states encompassed by the two arms of the coexistence line, the system is a mixture of the liquid and vapour phases. In the future, these calculations will be improved by using more precise interactions.

3 Perturbative Quantum MC Method for Nuclear Physics

Quantum Monte Carlo (QMC) simulations are a powerful method for addressing quantum many-body problems in many area of physics. Often, the so-called “sign problem” leads

to exponential scaling of the computational effort with system size. Despite this, there are a number of cases where QMC algorithms can be applied without sign problems (such as the leading-order SU(4) symmetric nuclear interaction used in the preceding section). The realistic systems of physical interests, though, often deviate from these ideal models significantly and have a sign problem. In these cases, perturbation theory can be used to bridge the difference between the simplified and the realistic interaction. However, in QMC perturbation theory is mostly limited to the first order. Improving the quality of the perturbative calculations requires going to higher orders. In Rayleigh-Schrödinger perturbation theory, the second-order energy correction involves a summation over all quantum states that can be reached via the perturbing interaction. Such a calculation over all quantum states is not compatible with QMC, which targets only the lowest energy state. Thus, a different approach is needed. To solve this problem, a new computational framework called perturbative QMC (ptQMC), which allows for the efficient calculation of higher-order perturbative corrections within the Euclidean time formalism, was introduced in Ref. 11. To be specific, consider the nuclear Hamiltonian given $H = K+V_0+V_C$, with $K = -\nabla^2/2m$ the kinetic energy operator and m the nucleon mass. The interaction is split into a dominant term V_0 and a correction V_C. The perturbative expansion of the energy takes the form $E = E_0 + \delta E_1 + \delta E_2 + \ldots$, where the indices $0, 1, 2, ...$ denote the leading order, the first order perturbative correction and so. The partial energy contributions at each order are

$$\begin{aligned} E_0 &= \langle\Psi_0|(K+V_0)|\Psi_0\rangle/\langle\Psi_0|\Psi_0\rangle\ ,\ \ \delta E_1 = \langle\Psi_0|V_C|\Psi_0\rangle/\langle\Psi_0|\Psi_0\rangle, \\ \delta E_2 &= \mathrm{Re}(\langle\Psi_0|V_C|\delta\Psi_1\rangle - \delta E_1\langle\Psi_0|\delta\Psi_1\rangle)/\langle\Psi_0|\Psi_0\rangle, \end{aligned} \tag{4}$$

where the wave function Ψ has a similar perturbative expansion

$$\begin{aligned} |\Psi\rangle &= \lim_{L_t\to\infty} M^{L_t/2}|\Psi_T\rangle = |\Psi_0\rangle + |\delta\Psi_1\rangle + \mathcal{O}(V_C^2), \\ |\Psi_0\rangle &= \lim_{L_t\to\infty} M_0^{L_t/2}|\Psi_T\rangle,\ |\delta\Psi_1\rangle = \lim_{L_t\to\infty}\sum_{k=1}^{L_t/2} M_0^{L_t/2-k}(M-M_0)M_0^{k-1}|\Psi_T\rangle, \end{aligned} \tag{5}$$

with $M_0 =: \exp\{-a_t(K+V_0)\}$: the zeroth order transfer matrix and the $\mathcal{O}(a_t^2)$ terms are omitted. Consequently, all matrix elements and overlaps can be expressed with the amplitudes,

$$\mathcal{M}(O) = \langle\Psi_T|M_0^{L_t/2}OM_0^{L_t/2}|\Psi_T\rangle, \tag{6}$$

$$\mathcal{M}_k(O) = \langle\Psi_T|M_0^{L_t/2}OM_0^{L_t/2-k}MM_0^{k-1}|\Psi_T\rangle, \tag{7}$$

where $k = 1, 2, \cdots, L_t/2$. Here O is the operator inserted in the middle time step like $1, K+V_0$ or V_C. In $\mathcal{M}_k(O)$ the k-th copy of M_0 is replaced by the full transfer matrix M. The transfer matrices M_0 and M in these amplitudes are computed using the auxiliary field formalism. The energies E_0 and δE_1 are just the expectation values $\langle O\rangle = \mathcal{M}(O)/\mathcal{M}(1)$ with $O = K+V_0$ or V_C. These can be calculated by sampling the auxiliary fields s in M_0 with standard algorithms. For δE_2 we need to evaluate the quotient $\mathcal{M}_k(O)/\mathcal{M}(1)$. What remains to be calculated is an integral over the auxiliary field c from the inserted M in $\mathcal{M}_k(O)$. For every sample $\{s_1, s_2, \cdots, s_{L_t}\}$ we have

$$\mathcal{M}_k(O) = \int \mathcal{D}cP(c+\bar{c})\langle\cdots O\cdots M(s_k, c+\bar{c})\cdots\rangle_T, \tag{8}$$

where the ellipses denote the transfer matrices $M_0(s_t)$ with $t \neq k$, $\langle\rangle_T$ the expectation value in the state $|\Psi_T\rangle$ and $P(c)$ is the standard normal distribution. In Eq. 8 we have made a variable change $c \to \bar{c} + c$ with c real integral variables. Here, $\bar{c}(\boldsymbol{n})$ is a constant field

$$\bar{c}(\boldsymbol{n}) = \frac{\partial}{\partial c(\boldsymbol{n})} \ln\langle \cdots M(s_k, c) \cdots \rangle_T \Big|_{c=0} = \sqrt{-a_t C}\langle \cdots : M_0(s_k)\rho_c(\boldsymbol{n}) : \cdots \rangle_T / \mathcal{M}(1), \tag{9}$$

where the ellipses again represent the M_0's, C is the coupling constant for the V_C term. Generally, $\bar{c}$ is a complex field, e.g., for repulsive interactions such as Coulomb we have $C > 0$, and the square root in Eq. 9 introduces an imaginary factor i. In this case the integrand in Eq. 8 contains non-zero phases that may induce a severe sign problem. The variable change in Eq. 8 serves to alleviate this problem[12]. To see this, we take the logarithm of the integrand in Eq. 8, expand the result near $c = 0$ and apply Eq. 9. We find that the terms linear in c and $\bar{c}$ which cause the sign problem cancel exactly and the integrand can be factorised as

$$\mathcal{M}_k(O) = \mathcal{M}(s) \exp\left(\frac{\bar{c}^2}{2}\right) \int \mathcal{D}c \exp\left(-\frac{c^2}{2} + \epsilon\right), \tag{10}$$

where we omit the sum over lattice sites, and ϵ is a residual term containing quadratic and higher powers of c. Because in $\mathcal{M}_k(s, c)$ a common factor $\sqrt{a_t}$ is attached to every c variable, ϵ is a small number of the order $\mathcal{O}(a_t)$. For sufficiently small a_t, Eq. 10 means that the integrand in Eq. 8 is a product of a normal distribution and a slowly varying function $\exp(\epsilon)$. We can use stochastic methods to evaluate Eq. 8 by sampling the c field with a standard normal distribution. This evaluation is unbiased and its uncertainty is determined

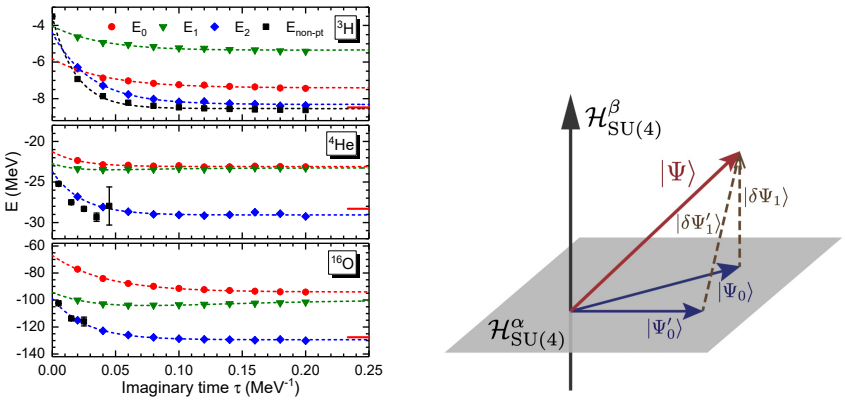

Figure 3. Left panel: ptQMC binding energies as functions of the projection time τ compared with non-perturbative results. The circles (red), down triangles (green) and diamonds (blue) denote the energies at the zeroth, first and second orders, respectively. The squares (black) represent the exact results calculated with sparse matrix multiplications for ^{3}H and full non-perturbative QMC for ^{4}He and ^{16}O, respectively. Each group of results are fitted with a sum of exponential functions (dashed lines). The red bars mark the experimental binding energies. Right panel: Schematic plot for a perturbative calculation. The zeroth order wave functions $|\Psi_0\rangle$ and $|\Psi'_0\rangle$ are confined in a subspace corresponding to an *irrep* of SU(4).

by the variation of $\exp(\epsilon)$. We benchmark the ptQMC using a realistic nuclear chiral force with two-body interactions up to N^{2}LO[13,14], for details see Ref. 11. In order to compute ground states of $H = K + V_{2\mathrm{N}} + V_{\mathrm{cou}}$ using ptQMC, the zeroth order Hamiltonian is $H_0 = K + V_0$ and one calculates the energy corrections with respect to $V_C = H - H_0$. V_0 is the non-locally smeared SU(4) interaction from Ref. 15, which is independent of the spin and isospin and captures the essential elements of the nuclear force. In the left panel of Fig. 3 we compare the results obtained using ptQMC with non-perturbative results. We use a periodic box of size $L = 10$ for ^{3}H and $L = 8$ for the other nuclei. The temporal step is $a_t = 1/1000$ MeV^{-1}. For ^{3}H, the system is small enough that we can use exact sparse matrix calculations. For larger nuclei this is not possible, and so we perform fully non-perturbative QMC calculations instead, which result in large error bars due to severe sign problems. For the ^{16}O nucleus, the sign problem sets in so quickly that we cannot find meaningful results for large τ to make a reliable extrapolation. However, the ptQMC calculations are free from sign problems. The corresponding statistical errors are smaller than the size of the symbols in the figure. A sum of decaying exponential functions is used to capture the residual effects of higher energy excitations and the results are extrapolated to $\tau \to \infty$. For all three nuclei, the second order energy corrections are large and essential in reproducing the data. While this might seem contrary to the normal expectation of the perturbative series, this is actually a consequence of the symmetry breaking. As the unperturbed Hamiltonian H_0 respects the SU(4) symmetry, the wave function $|\Psi_0\rangle$ must belong to one of its irreducible representations (*irreps*). The full Hamiltonian breaks the SU(4) symmetry, thus its ground state $|\Psi\rangle$ is a mixture of different SU(4) *irreps*. As is shown in the right panel of Fig. 3, the components of $|\Psi\rangle$ that mixes the SU(4) *irreps* can only be seen in $|\delta\Psi_1\rangle$ or δE_2. Note that this effect is strongest for the one-pion-exchange potential as it breaks both the Wigner-SU(4) and the spin SU(2) symmetries. Having found such a large second order correction, one must examine the perturbative series beyond second order. This can be done using the deuteron as an example. For the deuteron in a small periodic box, an explicit calculation shows that while the second order correction is sizable due to symmetry-breaking perturbations, higher orders beyond second order are small. This is consistent with the findings for heavier nuclei discussed above. For more general calculations, it is also possible that the higher orders have alternate signs and cancel with each other to give a small residual term. The method presented here is free from the sign problem and can be applied to QMC calculations for many-body systems in nuclear physics, condensed matter physics, ultracold atoms, and quantum chemistry.

4 Emergent Geometry of the Carbon Nucleus

The ^{12}C nucleus is under active investigations both experimentally and theoretically, but still there is little consensus about the nature of various excited states, like e.g. the famous Hoyle state, that was also studied in NLEFT[16,17]. There are two main impediments to reaching definitive conclusions about the structure of the low-lying ^{12}C states. The first is the inability to perform calculations that can handle strong multi-particle correlations. The second is the inability to measure the detailed spatial correlations required to determine the intrinsic structure of the twelve-particle wave function. In Ref. 18 both problems were addressed. The full twelve-particle correlations were calculated and a model-independent tomographic projection to determine the intrinsic three-dimensional structure of each nu-

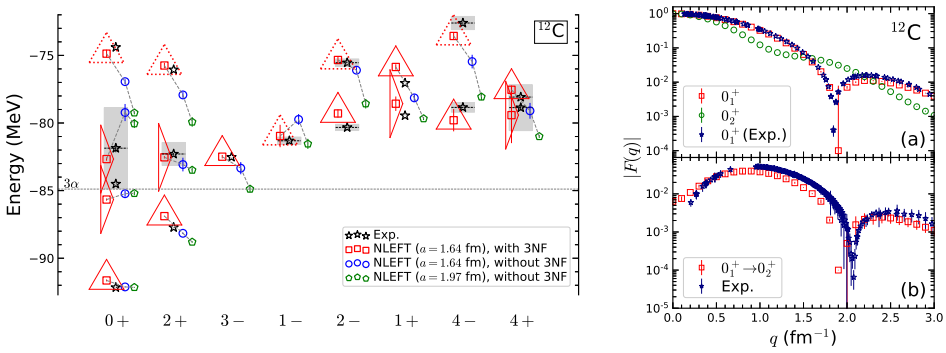

Figure 4. Left Panel: Spectrum of ^{12}C (red squares) in comparison with experimental (black stars). The error bars correspond to one standard deviation errors. The grey shaded regions indicate decay widths for cases where it has been measured. Earlier results for $a = 1.64$ fm (blue circles) and $a = 1.97$ fm (green pentagons) are also shown[20]. The triangular shapes indicate the intrinsic shape of each state, either equilateral or obtuse triangle arrangements of alpha clusters. The dotted lines for some equilateral triangles indicate significant distortions or large-amplitude displacements of the alpha clusters. Right Panel: The absolute value of the charge form factor $F(q)$ versus momentum transfer q. The top figure (a) shows the ground state (red squares) and Hoyle state (green circles), and the bottom figure (b) shows the transition from the ground state to the Hoyle state (red squares). The error bars correspond to one standard deviation errors. Experimental data (purple stars) are shown for comparison[22–25].

clear state was given. In these calculations, a simple SU(4) symmetric interaction was used, as in the description the ground state energies of light and medium-mass nuclei[15] and the thermodynamics of symmetric nuclear matter[2]. It also reproduces the low-energy spectrum of ^{12}C well[20]. This interaction involves four parameters, that are determined from a fit to the groundstate energies of ^{4}He and ^{12}C, the carbon charge radius and and to several electromagnetic transition rates. An assortment of different initial states for each state of ^{12}C is used to verify that the choice of initial state does not affect the final observables. The initial states considered include many different shell model states as well as different geometric configurations of alpha clusters. The pinhole algorithm is used to determine the probability distribution for the nucleon positions, spins, and isospins[3]. For each pinhole configuration, we know the positions of all A nucleons, and thus the position of each nucleon relative to the centre of mass is easily calculated. From this information, we can compute many nuclear observables like the charge density. The charge form factor $F(q)$ is then calculated by Fourier transforming the charge density. We have calculated the ^{12}C spectrum up to excitation energies of about 15 MeV for $a = 1.64$ fm. The results are plotted as red squares in the left panel of Fig. 4 for different values of the angular momentum and parity. For comparison we show the experimental data (black stars)[21] and earlier results, which were performed without three-nucleon forces[20]. Overall, the agreement with the empirical results is quite good. In the right panel of Fig. 4, the form factors for the ground state and the Hoyle state in the top figure (a), and the transition form factor from the ground state to the Hoyle state in the bottom figure (b) are shown compared to the corresponding experimental data. The agreement is fairly good. Using the pinhole algorithm, we can uniquely determine the three alpha clusters in each state. These three alpha clusters define a triangle

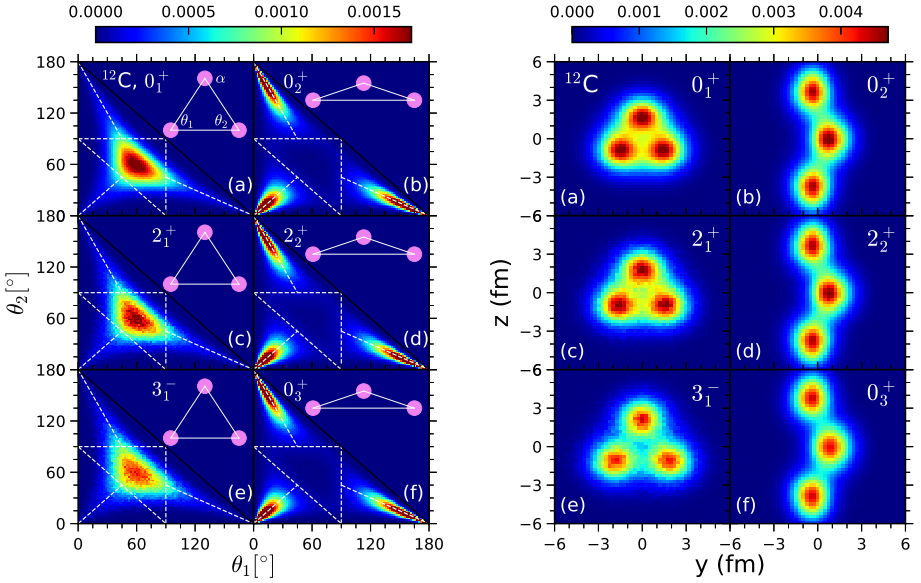

Figure 5. Nuclear density distributions for the (a) 0_1^+ ground state, (b) 0_2^+ Hoyle state, (c) 2_1^+, (d) 2_2^+, (e) 3_1^-, and (f) 0_3^+ states. The red (blue) colour signals a high (low) probability. Left Panel: Density distribution for the two inner angles of the triangle formed by the three alpha clusters. The two axes are for the two inner angles θ_1 and θ_2 measured in degrees. Right Panel: Tomographic projection of the nuclear density for different states of ^{12}C. In each case the orientation of the shortest root-mean-square direction is aligned with the x axis.

in three-dimensional space with interior angles θ_1, θ_2, and $180^\circ - \theta_1 - \theta_2$. In the left panel of Fig. 5, we show the probability distributions as a function of θ_1 and θ_2 for ground state an various excited states. The dashed white triangle formed by the line segments $\theta_1 = 90^\circ$, $\theta_2 = 90^\circ$, and $\theta_2 = 90^\circ - \theta_1$, represents cluster configurations that are right triangles. The interior region of the dashed white triangle corresponds to configurations that are acute triangles, and the exterior region corresponds to obtuse triangles. The other three white dashed line segments along the lines $\theta_1 = \theta_2$, $\theta_1 = \theta_3$, and $\theta_2 = \theta_3$ represent cluster configurations that are obtuse isosceles triangles. For the ground state, the probability distribution is strongly centred around an equilateral triangle, $\theta_1 = \theta_2 = \theta_3 = 60^\circ$. The 2_1^+ and 3_1^- states have similar equilateral triangular shapes. In contrast, the 0_2^+ Hoyle state corresponds to an obtuse isosceles triangle. This finding is consistent with older NLEFT studies[16,17]. The 2_2^+ and 0_3^+ states also have obtuse isosceles triangular shapes. We can also define a model-independent tomographic projection of the three-dimensional nuclear density for the states of ^{12}C, for details see Ref. 18 . In the right panel of Fig. 5, we show the density distribution of selected states of ^{12}C. The 0_1^+, 2_1^+, 3_1^-, 4_1^-, and 4_2^+ states have similar intrinsic equilateral triangular shapes, consistent with an interpretation as members of a rotational band built on top of the 0_1^+ state. The 0_2^+, 2_2^+, 4_1^+ states have similar intrinsic obtuse isosceles triangle shapes and are consistent with belonging to a rotational band built on top of the 0_2^+ state. These findings are consistent with previous studies based on group theoretical considerations[26]. We note that models where the Hoyle state has an equilateral

triangle symmetry predict an additional 3^- and 4^- state in the Hoyle state rotational band. The 0_3^+ state has been discussed as a breathing mode excitation of the Hoyle state[27–29], but its detailed structure remains a matter of debate. For example, in a recent work[27,28] the 0_3^+ and Hoyle states are suggested to have an equilateral triangular shape. A gas-like structure with a very large radius has also been predicted[29] for the 0_3^+ state. Our lattice findings suggest that the 0_3^+ state is a small-amplitude vibrational excitation of the Hoyle state. Our findings for the intrinsic shapes of the low-lying states of ^{12}C are summarised by the triangular shapes in the left panel of Fig. 4. Further studies using more precise interactions are planned.

5 Alpha-Alpha Scattering in the Multiverse

Alpha-alpha (α-α) scattering is one of the most fundamental reactions in nuclear (astro)physics. It features some fine-tuning, as the large near-threshold S-wave results from a state with $(J^P, I) = (0^+, 0)$ at an energy $E_R \simeq 0.1$ MeV above the threshold, see e.g. the review[30], with a tiny width of $\Gamma_R \simeq 6$ eV. It is precisely this small width (long lifetime) of the unstable ^{8}Be nucleus that allows for the reaction with the third α particle in the 3α reaction at sufficiently high temperatures and densities. Here, another fine-tuning appears, namely the closeness of the Hoyle state to the 3α threshold. The fine-tunings in these (and other) fundamental nuclear reactions together with other fine-tunings in particle physics and cosmology have led to the concept of the *Multiverse*, where our Universe with its observed values is part of a larger structure of universes featuring different sets of the fundamental constants. Related to this are anthropic considerations, which is the philosophical idea that the parameters governing our world should fit the intervals compatible with the existence of life on Earth. Coming back to nuclear physics, the closeness of the Hoyle state energy to the 3α threshold invites investigations about the stability of this resonance condition under changes of the fundamental parameters of the strong and the electromagnetic (em) interactions. This was already investigated in models, e.g. Ref. 31, and NLEFT[32–34]. The same chiral EFT at N2LO order combined with the so-called Adiabatic Projection Method (APM), that allows for *ab initio* calculations of nuclear reactions, as developed and applied in Refs. 35–39 can be used to study the sensitivity of the low-energy α-α phase shifts on variations in the light quark mass $\hat{m}$ and the em fine-structure constant $\alpha_{\rm EM}$[40]. While the investigation of the resonance enhancement in the 3α process due to the Hoyle state already sets rather stringent limits on the possible variations of the fundamental parameters, one has to be aware that these results are afflicted with some inherent uncertainties, as in the corresponding stellar simulations only the distance of the Hoyle state to the 3α-threshold is varied. Translating this into a dependence on, say, the light quark mass assumes that only the nuclei directly involved in the 3α process are subject to these changes, but of course one should perform the complete stellar simulations (reaction networks) with appropriately modified masses and reaction rates. At present, this is only possible for Big Bang Nucleosynthesis, but not for the whole nuclear reaction networks in stars. Therefore, the *ab initio* computation of the dependence of α-α scattering on the fundamental parameters of the Standard Model is not subject to such uncertainties and paves the way for more elaborate network calculations in the Multiverse. First, consider the physical values of the various coupling constants and masses (our Universe). Due to improvements in the APM compared to the pioneering study of α-α scattering in

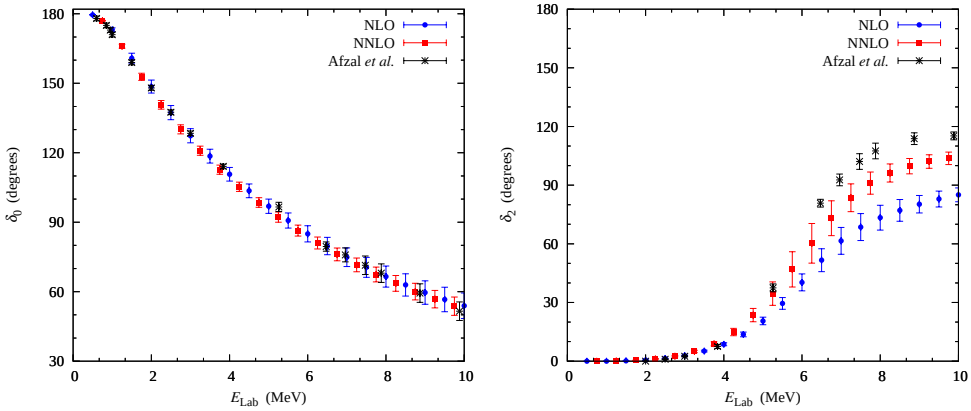

Figure 6. Left panel: S-wave α-α scattering phase shift δ_0 versus the energy in the laboratory system, $E_{\rm lab}$. Right panel: D-wave α-α scattering phase shift δ_2 versus the energy in the laboratory system, $E_{\rm lab}$. The blue circles and red squares represent the predictions at NLO and NNLO, respectively, while the data are given by the black crosses.

Ref. 38, we obtain a very good description of the S- and D-wave phase shifts up to energies $E_{\rm lab} \simeq 10\,$MeV at NNLO in the chiral expansion, see Fig. 6. For the study of the variations under changes of the pion mass with $|\delta M_\pi/M_\pi| \leq 10\%$, we rely on the pion mass dependent nuclear Hamiltonian worked out in Ref. 34. To this order, the ^{8}Be nucleus is slightly bound. In the S-wave phase shift, we find a dramatic effect (unbinding of the two-alpha system) for changes of -5% and -7% at NLO and NNLO, respectively. We have also considered the pion mass variation of the S-wave effective range function, which is less sensitive to the binding issue and shows an added repulsion for negative pion mass shifts. This additional repulsion will certainly impact the position and the lifetime of ^{8}Be. The pion mass variation on the D-wave is somewhat more pronounced, as seen by the effect on the corresponding resonance parameters and also by the D-wave effective range function. The dominant electromagnetic effect on the α-α scattering phase shifts is the long-ranged Coulomb potential that is included exactly by using a spherical wall with Coulomb boundary conditions. Taking this effect into account via the Coulomb-modified effective range expansion, we find very small effects of variations of $\alpha_{\rm EM}$ on the S- and D-wave phase shifts. We have further shown that up-to-and-including NLO in the chiral expansion, the dependence of the α-α scattering phase shifts on the QCD θ-angle is entirely given by the θ-dependence of the pion mass. In summary, we find that α-α scattering sets weaker constraints on the variation of the light quark masses and the fine-structure constant than that given by the closeness of the 3α threshold to the Hoyle state. However, as discussed in detail e.g. in Refs. 31, 34, this requires stellar modelling which introduces some model-dependence. In contrast to that, the investigation of α-α scattering discussed here is truly *ab initio* and not affected by such effects. Still, to further improve these calculations, a better determination of the pion mass dependence of the singlet and triplet NN scattering lengths from lattice QCD is mandatory.

6 Outlook: Towards N3LO Precision

At this time, NLEFT is a well-established *ab initio* framework at the forefront of the theory of nuclear structure and reactions. At present, high precision calculations at N3LO in the chiral counting are being performed. This is based on pinning down a precise leading order interaction as discussed in this contribution with SU(4) invariant interactions that are locally and non-locally smeared. In that way, the higher order corrections and higher few-nucleon forces can be treated in perturbation theory, as also discussed here. The underlying N3LO representation of the chiral two-nucleon force has already been worked out, see Ref. 41, and has been refined by including operators that restore Galilean invariance, see Ref. 42. First preliminary results for nuclei up to $A = 40$ have been reported e.g in Refs. 43, 44 and much more detailed and extended high-precision results not only for ground state energies, but also the spectrum of selected nuclei and the oxygen and calcium drip lines will be reported soon.

Acknowledgements

I thank my NLEFT colleagues for their contributions to the results presented here. This work is supported in part by the DFG (DFG Project ID 196253076 - TRR 110) through the funds provided to the Sino-German CRC 110 "Symmetries and the Emergence of Structure in QCD", by the Chinese Academy of Sciences (CAS) President's International Fellowship Initiative (PIFI) (grant no. 2018DM0034), by VolkswagenStiftung (grant no. 93562), and by the European Research Council (ERC) under the European Union's Horizon 2020 research and innovation programme (grant agreement No. 101018170, EXOTIC). The computational resources were provided by the Jülich Supercomputing Centre (JSC) at Forschungszentrum Jülich and by RWTH Aachen. Special resources on the JURECA-DC supercomputer at the JSC are particularly acknowledged.

References

1. T. A. Lähde and U.-G. Meißner, "Nuclear Lattice Effective Field Theory: An introduction," Lect. Notes Phys. **957**, 1-396, 2019.
2. B. N. Lu, N. Li, S. Elhatisari, D. Lee, J. E. Drut, T. A. Lähde, E. Epelbaum, and U.-G. Meißner, Phys. Rev. Lett. **125**, 192502, 2020.
3. S. Elhatisari *et al.*, Phys. Rev. Lett. **119**, 222505, 2017.
4. R. Blankenbecler, D. J. Scalapino, and R. L. Sugar, Phys. Rev. D **24**, 2278, 1981.
5. N. Byers and C. N. Yang, Phys. Rev. Lett. **7**, 46-49, 1961.
6. E. Y. Loh, Jr. and D. K. Campbell, Synthetic Metals **27**, A499, 1988.
7. R. Valenti, C. Gros, P. J. Hirschfeld, and W. Stephan, Phys. Rev. B **44**, 13203, 1991.
8. G. Hagen, T. Papenbrock, A. Ekström, K. A. Wendt, G. Baardsen, S. Gandolfi, M. Hjorth-Jensen, and C. J. Horowitz, Phys. Rev. C **89**, 014319, 2014.
9. B. Schuetrumpf, W. Nazarewicz, and P. G. Reinhard, Phys. Rev. C **93**, 054304, 2016
10. J. B. Elliott, P. T. Lake, L. G. Moretto, and L. Phair, Phys. Rev. C **87**, 054622, 2013.
11. B. N. Lu, N. Li, S. Elhatisari, Y. Z. Ma, D. Lee, and U.-G. Meißner, [arXiv:2111.14191 [nucl-th]].

12. S. Zhang and H. Krakauer, Phys. Rev. Lett. **90**, 136401, 2003.
13. E. Epelbaum, H. W. Hammer, and U.-G. Meißner, Rev. Mod. Phys. **81**, 1773, 2009.
14. P. Reinert, H. Krebs, and E. Epelbaum, Eur. Phys. J. A **54**, 86, 2018.
15. B. N. Lu, N. Li, S. Elhatisari, D. Lee, E. Epelbaum, and U.-G. Meißner, Phys. Lett. B **797**, 134863, 2019.
16. E. Epelbaum, H. Krebs, D. Lee, and U.-G. Meißner, Phys. Rev. Lett. **106**, 192501, 2011.
17. E. Epelbaum, H. Krebs, T. A. Lähde, D. Lee, and U.-G. Meißner, Phys. Rev. Lett. **109**, 252501, 2012.
18. S. Shen, T. A. Lähde, D. Lee, and U.-G. Meißner, [arXiv:2202.13596 [nucl-th]].
19. D. Lee, Prog. Part. Nucl. Phys. **63**, 117, 2009.
20. S. Shen, T. A. Lähde, D. Lee, and U.-G. Meißner, Eur. Phys. J. A **57**, 276, 2021.
21. J. H. Kelley, J. E. Purcell, and C. G. Sheu, Nucl. Phys. A **968**, 71, 2017.
22. I. Sick and J. S. Mccarthy, Nucl. Phys. A **150**, 631, 1970.
23. P. Strehl, Z. Phys. **234**, 416, 1970.
24. H. Crannell, X. Jiang, J. T. O'Brien, D. I. Sober, and E. Offermann, Nucl. Phys. A **758**, 399, 2005.
25. M. Chernykh, H. Feldmeier, T. Neff, P. von Neumann-Cosel, and A. Richter, Phys. Rev. Lett. **105**, 022501, 2010.
26. D. J. Marin-Lambarri, *et al.*, Phys. Rev. Lett. **113**, 012502, 2014.
27. K. C. W. Li, *et al.*, Phys. Rev. C **105**, 024308, 2022.
28. K. C. W. Li, *et al.* Phys. Lett. B **827**, 136928, 2022.
29. B. Zhou, A. Tohsaki, H. Horiuchi, and Z. Ren, Phys. Rev. C **94**, 044319, 2016.
30. S. A. Afzal, A. A. Z. Ahmad, and S. Ali, Rev. Mod. Phys. **41**, 273, 1969.
31. H. Oberhummer, A. Csoto, and H. Schlattl, Science **289**, 88, 2000.
32. E. Epelbaum, H. Krebs, T. A. Lähde, D. Lee, and U.-G. Meißner, Phys. Rev. Lett. **110**, 112502, 2013.
33. E. Epelbaum, H. Krebs, T. A. Lähde, D. Lee, and U.-G. Meißner, Eur. Phys. J. A **49**, 82, 2013.
34. T. A. Lähde, U.-G. Meißner, and E. Epelbaum, Eur. Phys. J. A **56**, 89, 2020.
35. M. Pine, D. Lee, and G. Rupak, Eur. Phys. J. A **49**, 151, 2013.
36. S. Elhatisari and D. Lee, Phys. Rev. C **90**, 064001, 2014.
37. A. Rokash, M. Pine, S. Elhatisari, D. Lee, E. Epelbaum, and H. Krebs, Phys. Rev. C **92**, 054612, 2015.
38. S. Elhatisari, D. Lee, G. Rupak, E. Epelbaum, H. Krebs, T. A. Lähde, T. Luu, and U.-G. Meißner, Nature **528**, 111, 2015.
39. S. Elhatisari, D. Lee, U.-G. Meißner, and G. Rupak, Eur. Phys. J. A **52**, 174, 2016.
40. S. Elhatisari, T. A. Lähde, D. Lee, U.-G. Meißner, and T. Vonk, JHEP **02**, 001, 2022.
41. N. Li, S. Elhatisari, E. Epelbaum, D. Lee, B. N. Lu, and U.-G. Meißner, Phys. Rev. C **98**, 044002, 2018.
42. N. Li, S. Elhatisari, E. Epelbaum, D. Lee, B. Lu, and U.-G. Meißner, Phys. Rev. C **99**, 064001, 2019.
43. N. Li, S. Elhatisari, E. Epelbaum, D. Lee, B. N. Lu, and U.-G. Meißner, PoS **CD2018**, 099, 2019.
44. S. Elhatisari, Springer Proc. Phys. **238**, 585, 2020.